

## Phase-Averaged Towed PIV Measurements for Regular Head Waves in a Model Ship Towing Tank

J. Longo, J. Shao, M. Irvine, L. Gui, and F. Stern  
Iowa Institute of Hydraulic Research  
The University of Iowa, Iowa City, IA, USA

PIV and Modeling Water Wave Phenomena  
Cambridge, UK  
17-19 April 2002

### ABSTRACT

Phase-averaged towed PIV measurements are made for regular head waves in a model-ship towing tank using both fixed and towed PIV systems in preparation for tests with a model ship. Data reduction and uncertainty assessment software are developed and tested for both calm water and long wave, low steepness conditions used in previous tests with surface combatant. The results are validated through comparisons with progressive wave theory.

### 1 INTRODUCTION

Focus of engineering fluid dynamics research is moving into unsteady flows in support of computational fluid dynamics (CFD) code development for simulation-based design with numerous natural and forced unsteady flow applications for aerospace, turbo machinery, and marine and ship hydrodynamics industries. Meeting this challenge requires significant advances in both CFD and experimental fluid dynamics (EFD).

Present interest is in unsteady viscous ship hydrodynamics in support of unsteady Reynolds-averaged Navier Stokes (RANS) code development. Authors have identified forward-speed diffraction problem, i.e., restrained body advancing in regular headwaves, as building block problem towards ultimate goal of physical understanding and simulation of viscous nonlinear seakeeping and 6DOF maneuvering. Approach is complementary CFD, EFD, and uncertainty assessment (UA). CFD is used to guide EFD, EFD is used for validation and model development, and lastly CFD is validated and fills in sparse data for complete documentation and diagnostics of flow. Initial CFD study was conducted by Rhee and Stern (1998) and validated using Wigley hullform EFD data from Journee (1992) for investigation of unsteady forces and moments. A concurrent EFD study involving detailed measurement (Gui et al., 2001b) and UA (Gui et al., 2001a) of the turbulent nominal wake boundary layer of naval combatant DTMB model 5415 geosym (model 5512) was completed for development and commissioning of a towed, particle image velocimetry (PIV) measurement system for the Iowa

Institute of Hydraulic Research (IIHR) towing tank. Both CFD and EFD efforts were then initiated to investigate unsteady forces and moments, wavefield, and flowfield for model 5512 in regular head waves [Gui et al., 2001c; Gui et al., 2002; Wilson and Stern (2002)] of which the EFD work was part of an international collaborative project between IIHR, INSEAN, and DTMB on EFD/CFD and uncertainty assessment for DTMB model 5415 (Stern et al., 2000). The remaining EFD task is procurement of the unsteady flowfield and UA for model 5512 at the nominal wake plane. The present study is precursory for this task and will provide documentation of the unsteady data-acquisition and reduction procedures along with detailed data of the incident headwave flowfield and comparisons with 2D progressive-wave theory for evaluation of the results herein.

### 2 TEST DESIGN

#### 2.1 Facility

The tests are conducted in the IIHR towing tank. The tank is 100 m long, 3.048 m wide and deep, and equipped with a drive carriage, plunger-type wavemaker, and moveable wave dampener system. The drive carriage houses a computer (PC) and data-acquisition instrumentation, and pushes a 5.5-m trailer which is used as a platform for the PIV system and point of attachment for models. The wavemaker is hydraulically driven and controlled with an MTS controller and LabView software. It is capable of producing a wide range of wavelengths ( $\lambda=0.5-6.0$  m) and wave steepnesses ( $Ak=0.025-0.3$ ) and can also generate irregular waves. The wave dampeners are raised and lowered from the carriage before and after runs and enable twelve- and twenty-minute intervals for steady and unsteady tests, respectively. A right-handed Cartesian coordinate system ( $x, y, z$ ) is used for the tests (Fig. 1). The origin is at the intersection of the calm free surface and midpoint of the PIV measurement area. The  $x, y, z$  axes are directed downstream, into the page, and upward, respectively. The coordinate system moves with the speed of the carriage, trailer, and PIV system  $U_c$ . PIV data is transformed into a wave-based coordinate system after defining the phase angle associated with each vector map.

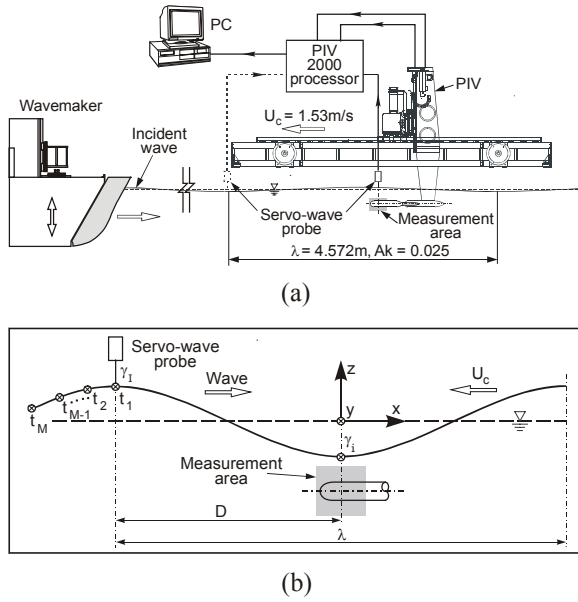


Fig. 1. Experimental setup showing: (a) wavemaker, PIV system, servo wave probe, model trailer, and incident head wave ( $\lambda=4.572$  m,  $A_k=0.025$ ); (b) coordinate system moving with camera.

## 2.2 Data-reduction equations

Measured variables are the steady and unsteady flowfield ( $U, V, W$ ) and elevation ( $z$ ). The data-reduction equation for steady or unsteady, instantaneous PIV measurements are expressed

$$C_{k,i,j} = \frac{L_{obj} S_{k,i,j}}{L_{img} \Delta t U_c} \quad (1)$$

$k = 1, 2, 3; i = 1, \dots, N_{vm}; j = 1, \dots, N_{cr}$

where  $L_{obj}$  is the width of the camera view in the object plane,  $L_{img}$  is the width of the digital image,  $S_{k,i,j}$  is the component of the particle image displacement, and  $\Delta t$  is the time between PIV images. The indices on  $C$  and  $S$  designate (1) velocity component:  $k=1, 2, 3$  for  $U, V, W$ , respectively; (2) vector map number:  $i=1, \dots, N_{vm}$  where  $N_{vm}$  is the total number of vector maps in a single carriage run; and (3) carriage run number:  $j=1, \dots, N_{cr}$  where  $N_{cr}$  is the total number of carriage runs for a single position of the PIV measurement area. The data-reduction equation for incident wave elevation is

$$\zeta_1(t) = \frac{z(t)}{L} \quad (2)$$

where  $L$  is the depth of the towing tank.

For unsteady PIV measurements, vector-map phase angle is defined

$$\gamma_{i,j} = -\gamma_{I_j} + \frac{D}{\lambda} 2\pi - \frac{t_i}{T_e} 2\pi \quad (3)$$

where  $\gamma_{I_j}$  is the 1<sup>st</sup>-harmonic phase angle of the  $j^{\text{th}}$ -incident wave,  $D$  is the distance between the servo wave gage and middle of the PIV measurement area,  $\lambda$  is the wavelength of

the incident wave,  $t_i$  is the time stamp of  $i^{\text{th}}$  vector map, and  $T_e$  is the encounter period.

Steady post-processed variables include mean values, normal stresses, and shear stresses expressed below in equations (4)-(6), respectively.

$$C_k = \frac{L_{obj}}{L_{img} \Delta t U_c} \frac{1}{N_{valid}} \sum_{ij=1}^{N_{valid}} S_{k,ij} = \frac{L_{obj}}{L_{img} \Delta t U_c} S_k \quad (4)$$

$$\overline{c_k c_k} = \frac{1}{N_{valid}} \sum_{ij=1}^{N_{valid}} (C_{k,ij} - C_k)^2 \quad k = 1, 2, 3 \quad (5)$$

$$\overline{c_m c_n} = \frac{1}{N_{valid}} \sum_{ij=1}^{N_{valid}} (C_{m,ij} - C_k)(C_{n,ij} - C_k) \quad (6)$$

$n = 1, 2, 3; m \neq n$

$N_{valid}$  is the number of valid vectors at any given grid point in the measurement area which remain after applying one or more filters to  $N_{vm} * N_{cr}$  data values.

Unsteady post-processed variables include encounter frequency ( $f_e$ ) and  $N^{\text{th}}$ -order Fourier series (FS) coefficients for wave elevation data and mean and turbulent PIV data.  $f_e$  is computed with a standard fast-Fourier transform (FFT) of the  $\zeta_1(t)$  time history. Next, FS analysis is performed on  $\zeta_1(t)$  to determine the phase of the incident wave at  $t=0$  sec. Finally, the generalized  $N^{\text{th}}$ -order FS for given variable  $X$  ( $X=\zeta, U, V, W, uu, vv, ww, uv, uw$ ) is applied as below

$$X_F(t) = \frac{X_0}{2} + \sum_{n=1}^N X_n \cos(2\pi n f_e t + \Delta\gamma_n) \quad (7)$$

$$\Delta\gamma_n = \gamma_n - \gamma_1 \quad (8)$$

$$X_n = \sqrt{a_n^2 + b_n^2} \quad (9)$$

$$\gamma_n = \tan^{-1}\left(\frac{b_n}{a_n}\right) \quad (10)$$

$$a_n = \frac{2}{T} \int_0^{T'} X(t) \cos(2\pi n f_e t) dt \quad \text{for } n = 0, 1, 2, \dots \quad (11)$$

$$b_n = \frac{2}{T} \int_0^{T'} X(t) \sin(2\pi n f_e t) dt \quad \text{for } n = 0, 1, 2, \dots \quad (12)$$

wherein  $X_F$  is the reconstructed time history;  $X_n$  is the  $n^{\text{th}}$ -order harmonic amplitude;  $\gamma_n$  is the corresponding phase;  $N$  is the order of the FS and chosen high enough to include all important frequency components.  $\Delta\gamma_n$  is the harmonic phase adjusted with the incident wave. Time interval  $T'$  is a multiple of the encounter wave period  $T_e (=1/f_e)$ . Turbulent fluctuations for the unsteady case are defined similarly as in equations (5) and (6), however, the FS reconstruction of  $U, V, W$  is substituted for the ‘‘mean’’ value,  $C_k$ .

## 2.3 Measurement systems

The towed DANTEC PIV system combines hardware and software that are integrated into a single measurement system illustrated in Fig. 1. The PIV hardware components

(hydrodynamic strut, laser, light-guiding arm, light-sheet optics, digital camera) are assembled with a massive 2D, computer-controlled traversing system capable of automated movement along the transverse (y) and vertical (z) axes. Movement in the x-coordinate is done manually. The strut is pressurized, partly submerged, and contains a 20 mJ, dual cavity Nd:Yag laser and light-guide arm for steering 532 nm beams through the light-sheet optics, which are housed in a submerged, streamlined torpedo. The digital camera is a 1K×1K (1008×1018 pixels) cross-correlation camera fitted with a f/1.4 50 mm lens that views the light sheet from a distance of 50 cm through a 90° mirror. The maximum object-plane size or MA is 7.5×7.5 cm<sup>2</sup>, however, smaller areas can be utilized to increase processor throughput. The camera is housed in a separate submerged, streamlined torpedo. Light-sheet and camera torpedoes are joined with a rigid, streamlined mini-strut such that the light sheet is orthogonal to the viewing axis of the camera. Fig. 1 shows the system configured to measure the vertical (xz) plane wherein mean (U, W) and turbulent ( $uu, ww, uw$ ) variables are acquired. Counter-clockwise rotation downward through 90° of the torpedoes and mini-strut about the light sheet torpedo longitudinal axis enables measurements in horizontal (xy) plane wherein mean (U, V) and turbulent ( $uu, vv, uv$ ) variables are acquired. Synchronization of the laser and camera, image processing, and acquisition of towing carriage speed are performed with the DANTEC PIV 2000 processor which is equipped with a four-channel, 12-bit analog-to-digital (AD) card. Data acquisition and parameter settings are facilitated with an IBM-compatible, Windows NT PC equipped with a National Instruments GPIB card and DANTEC v.3.11 Flowmanager software. Results in the form of vector maps are displayed virtually in real-time at a rate of 7.5 Hz. Unsteady data is phase-locked to the incident wave elevation by connection of a servo wave probe to the PIV AD board. The probe monitors the incident wave either directly above the MA or from some distance D upstream of the MA. The servo probe is a ±5 cm, pre-calibrated Kenek wave probe with a resolution of 0.1 mm and maximum probe velocity of 700 mm/s. Silver-coated hollow glass spheres with a density of 1600 kg/m<sup>3</sup> and an average diameter of 15 μm are used as seed particles. These particles have demonstrated very good light-reflectance for PIV image capture and adequate suspension capability. Additionally, the particles are capable of following sinusoidal motions with frequencies up to 1375 Hz.

The second measurement system is composed of a DOS PC and the IIHR speed circuit. This measurement system is used for monitoring and measuring the carriage speed for each data-acquisition run. The DOS PC also monitors the output from the servo wave probe.

## 2.4 Conditions

Steady (without wave) and unsteady (with wave) tests are performed with forward speed,  $U_c=1.53$  m/s. For unsteady cases, the head wave parameters including wavelength, frequency, and steepness are  $\lambda=4.572$  m,  $f_w=0.584$  Hz, and  $Ak=0.025$ , respectively, where  $f_w$  and  $Ak$  are defined in equations (13) and (14), and  $A$  and  $g$  are wave amplitude and local gravity acceleration ( $g=9.8031$  m/s<sup>2</sup>), respectively.

$$f_w = \sqrt{\frac{g}{2\pi\lambda}} \quad (13)$$

$$Ak = \frac{2\pi A}{\lambda} \quad (14)$$

The wave parameters and non-zero forward speed cases combine to produce an encounter frequency

$$f_e = \sqrt{\frac{g}{2\pi\lambda}} + \frac{U_c}{\lambda} \approx 0.922 \text{ Hz} \quad (15)$$

which is the dominant frequency of the unsteady response in the incident head wave flowfield. The above speed and wave conditions are based on Gui et al. (2001b), Gui et al. (2001c), and Gui et al. (2002).  $U_c=1.53$  m/s produces a Froude number  $Fr = U_c / \sqrt{gL_{pp}} = 0.28$  for testing with model 5512 which is the cruise speed for full-scale version. The wave parameters were selected following observation and analysis of unsteady forces and moment results because these parameters produced the most manageable linear response in the farfield of the ship model.

## 2.5 Data acquisition (DA) setup and procedures

Measurement area dimensions are 1008×1018 pixels (74.5×74.9 mm) and 192×1018 pixels (14.3×74.9 mm) for wide (WMA) and narrow (NMA), respectively. WMA captures significantly more area and data, and NMA has 18% the area of WMA. However, NMA was used for study of Gui et al. (2001b), has higher data throughput, and will later be shown to crop unwanted amplitude and phase errors in the unsteady data with forward speed. For WMA, DA parameters include 32×32 pixel interrogation areas, no overlap, 8 pixels of offset in the axial direction to account for strong axial component, and no window function. For NMA, DA parameters include 32×32 pixels, 50% overlap in both coordinates, 8 pixels of offset in the axial coordinate, and a Gaussian window function is used in the correlations. DA parameters for NMA yielded highest quality data. The final vector numbers are 31×31 and 11×62 for WMA and NWA, respectively. PIV image pairs are taken at 133 ms intervals, i.e., 7.5 Hz data rate and time between images is  $\Delta t=490\mu\text{s}$  and  $16170\mu\text{s}$ , for cases with and without forward speed, respectively. DOS data is sampled for 10 seconds over two analog channels at a rate of 410 Hz.

For WMA and the xz configuration,  $z=-25.0, -62.5, -100.0, -137.5, \text{ and } -175.0$  mm where the second and fourth elevations provide 50% overlap with the first and third and

third and fifth elevations, respectively, and the values are taken from the calm free surface to the top of the MA. Incident wave amplitude is 18.0 mm which means shallowest lightsheet elevation places top of MA 7.0 mm beneath wave troughs. For the xy configuration data is taken at  $z=-25.0$ ,  $-62.5$ , and  $-137.5$  mm. For NMA and the xz configuration,  $z=-25.0$ ,  $-53.34$ , and  $-110.45$  mm where the second elevation provides roughly 66% and 33% overlap with the first and third elevations, respectively. For the xy configuration data is taken at  $z=-25.0$  mm. For the unsteady cases, incident wave data is taken directly over the center of the measurement area (WMA) and 4.42 m upstream of the measurement area midpoint (NMA).

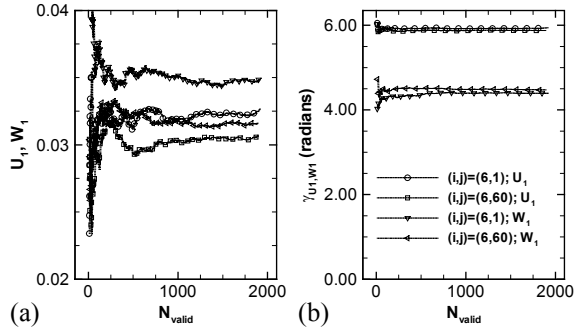


Fig. 2. Typical convergence histories of 1<sup>st</sup>-harmonic amplitude (a) and 1<sup>st</sup>-harmonic phase for U, W at two grid points.

For unsteady DA, first reference voltages for the servo probe and speed circuit are measured, then sidewall dampeners are raised, and the wavemaker is started and allowed to push a fully developed train of waves across the length of the tank. The carriage is started and reaches a steady speed after which PIV acquisition is initiated from the PC keyboard. The laser enters a free-running, 15 Hz mode. For each double image, the PIV processor makes one sweep across the analog inputs which includes the output from the servo wave probe ( $\zeta_i$ ) and correlates the digital images. The DOS computer runs in parallel with PIV windows machine, acquiring carriage speed and incident wave data. Vector maps are stockpiled over several carriage runs at a rate of 200 maps per carriage run. Convergence histories (Fig. 2) reveal that roughly 1200 and 2000 vector maps are required for steady and unsteady tests, respectively, for converged FS harmonics of mean and turbulence variables. For steady DA, same procedures apply except the wavemaker remains stationary.

## 2.6 Data reduction (DR) procedures

Data is post-processed with unsteady and steady FORTRAN 90 source codes written and executed from a Windows PC. A flowchart (Fig. 3) illustrates the major steps in processing the unsteady data. For unsteady DR, data is phase averaged by processing batches of carriage runs. Datasets (PIV and DOS speed files) are grouped by elevation and read as input (Fig. 4a).

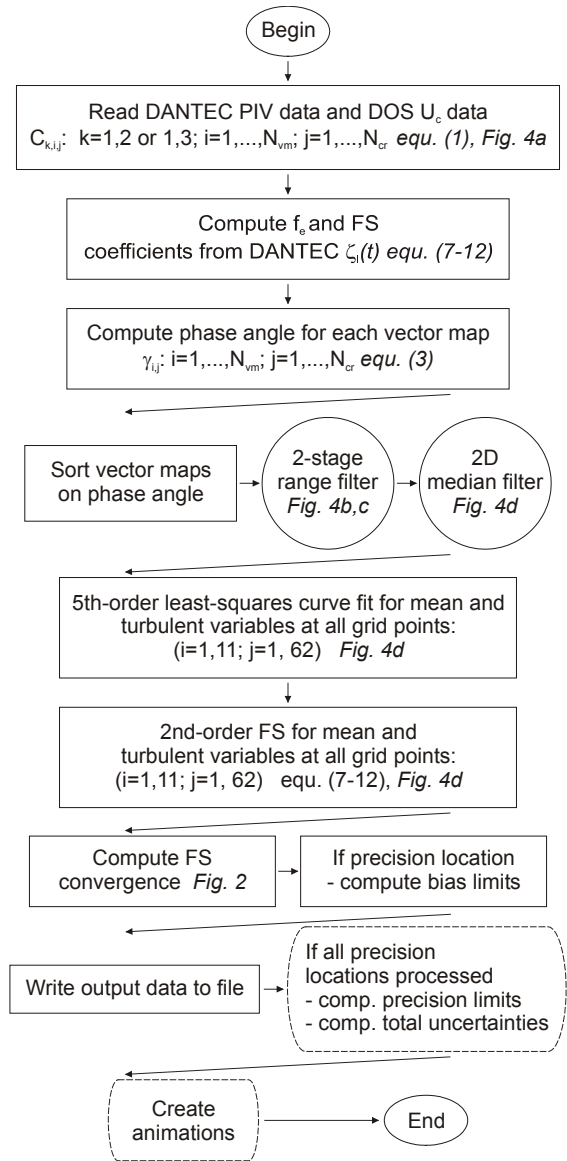


Fig. 3. Flowchart for unsteady PIV data processing. Dashed lines indicate final results.

Instantaneous PIV components are scaled up 1.2% with a scale-factor derived from uniform flow (i.e., no model, no model condition) tests.  $f_c$  is computed from DANTEC-sampled  $\zeta_i$  for each carriage run and FS coefficients are then computed which yields first-harmonic phase at  $t=0$  sec and wave amplitude.  $f_c$  is then used in equation (3) to compute specific phase angle of all vector maps in each carriage run. The following procedures are completed at each grid point in the MA. Data is sorted on phase angle from  $0-2\pi$  (Fig. 4b) and then filtered with a two-stage range filter and 2D-median filter to remove spurious vectors (Fig. 4b,c). Rejected vectors are not replaced because the phase-averaging technique does not require this step. A 5<sup>th</sup>-order least-squares curve is fit to the filtered data which represents the average unsteady response through one encounter period. Then, a 2<sup>nd</sup>-order FS is computed of the least-

squares curve fit to obtain the harmonic amplitudes and phases of the mean response (Fig. 4d). Next, turbulence quantities are computed for valid vectors by taking differences between raw data and the 2<sup>nd</sup>-order FS reconstruction (Fig. 4e). A 5<sup>th</sup>-order least squares curvefit is applied to this dataset. Finally, a 2<sup>nd</sup>-order FS is computed of the least-squares curve fit to obtain the harmonic amplitudes and phases of the turbulence response (Fig. 4f).

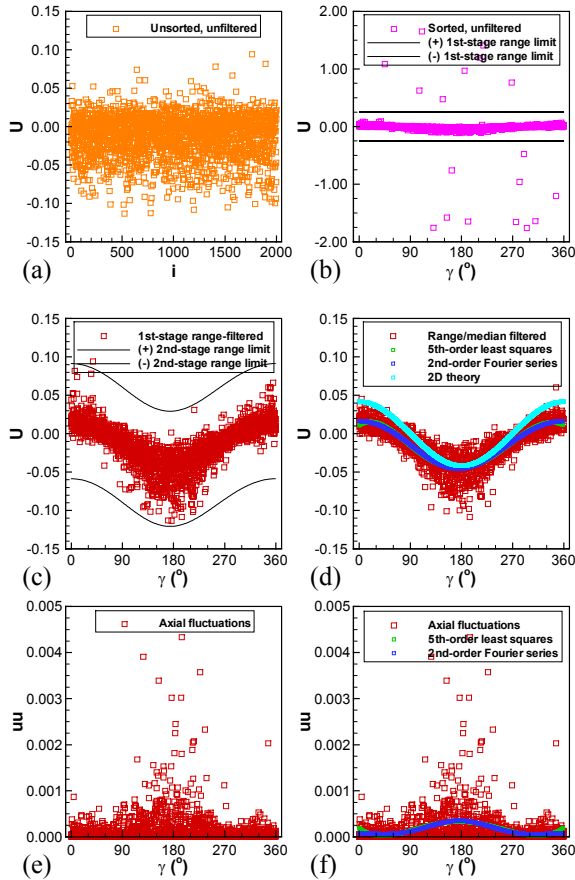


Fig. 4. Typical unsteady PIV data and data-reduction processes: (a) unsorted, unfiltered data; (b) phase-sorted, unfiltered data and 1<sup>st</sup>-stage range-filter limits; (c) 1<sup>st</sup>-stage range-filtered data and 2<sup>nd</sup>-stage range-filter limits; (d) range- and median-filtered data and least-squares, FS, and 2D theory comparison data; (e) axial fluctuations; (f) harmonic analysis of axial fluctuations.

For steady DR, data is also reduced by processing batches of carriage runs. Data is read and spurious vectors are removed with a two-stage range filter and a 3D median filter where the third dimension is time. Mean and turbulence results are computed with statistical analysis at each grid point from the full population of valid vectors. Convergence histories for each variable are computed  $N_{\text{valid}}-1$  times at seven equally spaced locations on the center of the MA from top to bottom.

## 2.7 Uncertainty assessment

The uncertainty assessment of the measurement results follows the ASME Test Uncertainty (1998). The UA procedures are based on separation and identification of systematic (bias) and random (precision) error sources, and combination with a root-sum-square (RSS) procedure to determine total uncertainty. 95% confidence levels are maintained for both bias and precision limits through judicious selection of individual bias error sources and small-sample ( $M=10$ ) multiple test approach for precision errors.

### 2.7.1 Background

Original development of UA procedures for steady PIV measurements were undertaken to commission the IIHR towed PIV system and document the quality of nominal wake data (Gui et al. 2001b). This effort produced a related study that assessed a technique for reducing the PIV cross-correlation evaluation bias with window functions (Gui et al. 2001a). UA for unsteady forces and moments and wavefield were then developed using same framework as for above PIV studies (Gui et al. 2001c; Gui et al. 2002). Present study requires development of all-new software for unsteady PIV UA, combining many of the ideas and concepts from above three studies for completion. Since much of the bias and precision limit code for unsteady PIV UA overlaps with steady PIV UA, all-new subroutines were developed for steady PIV UA. These were tested satisfactorily on the previous steady PIV dataset to evaluate new software for accuracy.

The steady UA is completed on the current PIV dataset for the  $xz$ -configuration and presented in the next section with comparisons previous UA values from Gui et al. 2001b. The unsteady UA is then outlined at two levels including the FS harmonics and the FS-reconstructed time histories and includes the equations and methodology. The UA procedures for FS harmonics and FS-reconstructed time histories will be discussed, and a summary of results for current measurements is provided.

### 2.7.2 Steady UA

Measurement uncertainties for the steady mean and turbulence variables are provided in Table 1 including previous values from Gui et al. (2001b). Bias and precision limit contributions are applicable to current results, only. Current results are considered satisfactory and show 1-3% reduced uncertainties over previous values for six of eight variables with  $w$  and  $uv$  moderately higher in magnitude than previous values. UA reductions are generally attributed to better repeatability of measurements, i.e., lower precision limits. For all quantities except shear stress, more than half of the uncertainty is attributed to the bias limits which is expected since uniform flow tests are low-turbulence cases.

Table 1. UA summary for steady-flow results.

Term	$B_x$	$P_x$	$U_x$	$\dagger U_x$
$U$	98.8%	1.2%	1.0%	2.4%
$V$	-	-	-	7.7%
$W$	99.8%	0.2%	3.1%	4.4%
$\overline{uu}$	99.8%	0.2%	2.0%	4.7%
$\overline{vv}$	-	-	-	-
$\overline{ww}$	99.6%	0.4%	2.9%	5.0%
$\overline{uv}$	-	-	-	-
$\overline{uw}$	32.1%	67.9%	0.1%	5.8%

†: results from Gui et al. 2001b

### 2.7.3 Unsteady UA

In order to determine the bias limits for the FS harmonic amplitudes and phases, it is assumed that the measured value  $X$  deviates from the real value  $X'$  with a bias error  $\beta$ . When the random error is not considered, the real and measured value are related with

$$X = X' + \beta \quad (16)$$

The bias error  $\beta$  is not a constant, and it is usually a function of the measurement value. For simplification, we assume the relation is linear, i.e.

$$\beta = \beta_0 + \kappa X' \quad (17)$$

where  $\kappa$  is the bias gradient, and  $\beta_0$  is the constant part of the bias error. The FS harmonic amplitudes and phases ( $n \neq 0$ ) for the biased and unbiased cases are related as follows:

$$\begin{aligned} a_n &= \frac{2}{T'} \int_0^{T'} (1 + \kappa) X'(t) \cos(2\pi n f t) dt + \frac{2}{T'} \int_0^{T'} \beta_0 \cos(2\pi n f t) dt \\ &= (1 + \kappa) \frac{2}{T'} \int_0^{T'} X'(t) \cos(2\pi n f t) dt + 0 = (1 + \kappa) a'_n \end{aligned} \quad (18)$$

$$b_n = (1 + \kappa) b'_n \quad (19)$$

$$X_n = \sqrt{a_n^2 + b_n^2} = (1 + \kappa) X'_n \quad (20)$$

$$\gamma_n = \tan^{-1} \left( \frac{(1 + \kappa) b'_n}{(1 + \kappa) a'_n} \right) = \tan^{-1} \left( \frac{b'_n}{a'_n} \right) = \gamma'_n \quad (21)$$

Wherein  $a'$ ,  $b'$ ,  $X'_n$  and  $\gamma'$  are for the unbiased case. The bias errors for the FS harmonic amplitudes and phases can then be determined as

$$\beta_{X_n} = X_n - X'_n = \frac{\kappa}{1 + \kappa} X_n \quad (22)$$

$$\beta_{\gamma_n} = \gamma_n - \gamma'_n = 0 \quad (23)$$

The above deductions indicate that the bias error of the FS harmonic amplitude does not directly depend on the bias error, but on the bias gradient of the measured variable. Also, the bias error of the FS harmonic phase is independent of the bias error of the measured variable  $X$ . According to equation (22) the bias limits of the FS harmonic amplitudes can be determined as

$$B_{X_n} = \frac{\kappa^*}{1 + \kappa^*} X_n \quad \text{for } n \neq 0 \quad (24)$$

where  $\kappa^*$  is the limit (maximal magnitude) of the bias gradient, which can be calculated with the data-reduction equation and elementary bias limits. The bias limit of the zeroth FS harmonic amplitude is determined as

$$B_{X_0} = \frac{2}{T'} \int_0^{T'} B_X dt = 2 \overline{B_X} \quad (25)$$

According to equation (23) the bias limits of the FS harmonic phases equal zero, i.e.  $B_{\gamma_n} = 0$ . The bias limits of the adjusted phases ( $B_{\Delta\gamma_n}$ ) are then determined with equation (3). For example, the bias limits of the 1<sup>st</sup>-harmonic phases for  $U$ ,  $V$ ,  $W$  are written

$$\begin{aligned} B_{\Delta\gamma_{U,n}} &= B_{\Delta\gamma_{V,n}} = B_{\Delta\gamma_{W,n}} = \\ &= \sqrt{(\theta_D B_D)^2 + (\theta_\lambda B_\lambda)^2 + (\theta_t B_t)^2 + (\theta_{Te} B_{Te})^2} \end{aligned} \quad (26)$$

The precision limits of the FS harmonics are determined with the multiple-test method. Ten converged xz-configuration unsteady datasets are obtained at  $z = -25.0$  mm. The datasets are spaced in time through the course of the experiments to account for factors that influence the precision of the measured variables such as ambient motions in the tank water, laser-power variability, seeding variability, etc. The precision limits are computed with

$$P_X = \frac{K \cdot St_X}{\sqrt{M}} \quad (27)$$

where  $K=2$  is the coverage factor for 95% confidence level and  $St_X$  is the standard deviation of the sample of  $M=10$  realizations of variable  $X$ . The total uncertainty for the measured variables  $U_X$  is defined as the RSS of the bias and precision limits and normalized with the dynamic range of the variable.

$$U_X = \sqrt{B_X^2 + P_X^2} \quad (28)$$

Uncertainties in Tables 1, 2, and 3 represent average values from 62 locations ( $i=6, j=1-62$ ) on the measurement grid.

The data-reduction equation for a FS-reconstructed time history can be represented as

$$X_F(t) = X_F(X_0, X_1, X_2, \dots, X_N, \Delta\gamma_1, \Delta\gamma_2, \dots, \Delta\gamma_N, t) \quad (29)$$

For the reconstructed time history, time  $t$  is a given value, so it has neither bias nor precision errors. According to the data-reduction equation the bias and precision limits are determined with

$$B_{X_F} = \sqrt{(\theta_{X_0} B_{X_0})^2 + \sum_{n=1}^N (\theta_{X_n} B_{X_n})^2 + \sum_{n=1}^N (\theta_{\Delta\gamma_n} B_{\Delta\gamma_n})^2} \quad (30)$$

$$P_{X_F} = \sqrt{(\theta_{X_0} P_{X_0})^2 + \sum_{n=1}^N (\theta_{X_n} P_{X_n})^2 + \sum_{n=1}^N (\theta_{\Delta\gamma_n} P_{\Delta\gamma_n})^2} \quad (31)$$

The sensitivity coefficients are

$$\theta_{X_0} = \frac{\partial X_F}{\partial X_0}, \theta_{X_n} = \frac{\partial X_F}{\partial X_n}, \theta_{\Delta\gamma_n} = \frac{\partial X_F}{\partial \Delta\gamma_n} \quad (32)$$

Total uncertainties for the reconstructed time histories are computed as per the FS harmonics in equation (28).

Table 2. UA summary for U,W FS harmonics.

Term	$B_x$ (%)	$P_x$ (%)	$U_x$ (%)
$U_0$	0.6402E-02 (98.3)	0.8438E-03 (1.7)	0.6457E-02 (1.1)
$W_0$	0.4872E-02 (99.4)	0.3856E-03 (0.6)	0.4887E-02 (3.1)
$\overline{uu}_0$	0.1153E-03 (94.3)	0.2848E-04 (5.7)	0.1188E-03 (2.2)
$\overline{ww}_0$	0.5817E-04 (78.9)	0.3010E-04 (21.1)	0.6550E-04 (3.2)
$\overline{uw}_0$	0.1226E-05 (28.2)	0.1957E-05 (71.8)	0.2310E-05 (0.1)
$U_1$	-0.5905E-03 (20.6)	0.1160E-02 (79.4)	0.1301E-02 (1.4)
$W_1$	-0.6506E-03 (50.4)	0.6451E-03 (49.6)	0.9162E-03 (2.4)
$\overline{uu}_1$	-0.9188E-06 (0.1)	0.2703E-04 (99.9)	0.2704E-04 (0.8)
$\overline{ww}_1$	-0.3469E-06 (0.2)	0.6996E-05 (99.8)	0.7005E-05 (0.9)
$\overline{uw}_1$	-0.1618E-06 (0.6)	0.2155E-05 (99.4)	0.2161E-05 (0.3)
$U_2$	-0.1397E-04 (0.2)	0.3203E-03 (99.8)	0.3206E-03 (1.1)
$W_2$	-0.1229E-04 (0.4)	0.1860E-03 (99.6)	0.1864E-03 (1.1)
$\overline{uu}_2$	-0.3475E-06 (0.1)	0.9180E-05 (99.9)	0.9187E-05 (0.5)
$\overline{ww}_2$	-0.4004E-06 (0.2)	0.9408E-05 (99.8)	0.9416E-05 (3.2)
$\overline{uw}_2$	-0.2245E-06 (1.4)	0.1897E-05 (98.6)	0.1911E-05 (0.6)
$\gamma_{U_1}$	0.3592E+00 (99.2)	0.3284E-01 (0.8)	0.3607E+00 (5.7)
$\gamma_{W_1}$	0.3592E+00 (99.7)	0.1964E-01 (0.3)	0.3598E+00 (5.7)
$\gamma_{\overline{uu}_1}$	0.3626E+00 (92.9)	0.1000E+00 (7.1)	0.3761E+00 (6.0)
$\gamma_{\overline{ww}_1}$	0.4161E+00 (61.4)	0.3303E+00 (38.6)	0.5313E+00 (8.5)
$\gamma_{\overline{uw}_1}$	0.7430E+00 (29.7)	0.1143E+01 (70.3)	0.1364E+01 (21.7)
$\gamma_{U_2}$	0.4750E+00 (17.0)	0.1049E+01 (83.0)	0.1151E+01 (18.3)
$\gamma_{W_2}$	0.4750E+00 (46.2)	0.5123E+00 (53.8)	0.6987E+00 (11.1)
$\gamma_{\overline{uu}_2}$	0.5177E+00 (5.3)	0.2178E+01 (94.7)	0.2239E+01 (35.6)
$\gamma_{\overline{ww}_2}$	0.3707E+00 (81.6)	0.1761E+00 (18.4)	0.4104E+00 (6.5)
$\gamma_{\overline{uw}_2}$	0.4577E+00 (46.0)	0.4961E+00 (54.0)	0.6750E+00 (10.7)

†: normalized with  $X_1$ ; ‡: normalized with  $2\pi$

Table 3. UA summary for reconstructed time histories of U,W.

Term	$B_x$ (%)	$P_x$ (%)	$U_x$ (%)
$U_F(t)$	0.6432E-02 (94.6)	0.1533E-02 (5.4)	0.6612E-02 (1.0)
$W_F(t)$	0.4921E-02 (97.3)	0.8139E-03 (2.7)	0.4988E-02 (2.5)

Measurement uncertainties for the FS harmonics including 0<sup>th</sup>, 1<sup>st</sup>, 2<sup>nd</sup> harmonic amplitude, 1<sup>st</sup>, 2<sup>nd</sup> harmonic phase are provided in Table 2. As expected, comparisons of

steady and 0<sup>th</sup>-harmonic uncertainties are close for all variables since bias terms are the same and dynamic ranges are similar. For all variables except shear stress, bias limits are the dominant sources of uncertainty. First- and 2<sup>nd</sup>-harmonic amplitude uncertainties are judged satisfactory in consideration of their smaller dynamic ranges. For nearly all 1<sup>st</sup>- and 2<sup>nd</sup>-harmonic amplitude variables, precision limits contribute 80-99% to total uncertainty. First-harmonic phase uncertainties are moderate with large contribution of bias limit to total uncertainty in four of five variables. 95% of the bias limit for these variables is associated with the bias limit in  $T_e$ . Several 2<sup>nd</sup>-harmonic phase uncertainties are increased over 1<sup>st</sup>-harmonic counterparts. The multiple test results for this low-turbulence application suggest that 2<sup>nd</sup>-harmonic amplitude content is difficult to reproduce in a series of converged datasets, i.e., precision limits account for nearly 100% of total uncertainty in 2<sup>nd</sup>-harmonic amplitude uncertainties. This effect manifests as higher uncertainties in 2<sup>nd</sup>-harmonic phase variables and high contribution of precision limit to total uncertainty in four of five variables.

Measurement uncertainties for the FS-reconstructed time histories are provided in Table 3. These values combine influences of uncertainties in 0<sup>th</sup>, 1<sup>st</sup>, 2<sup>nd</sup> harmonic amplitudes and 1<sup>st</sup>, 2<sup>nd</sup> harmonic phases. All uncertainties are judged satisfactory with highest accuracy in the axial coordinate as expected since signal-to-noise ratios for this measurement are consistently higher than for W. Bias limits are weighted higher than precision limits for both  $U_F(t)$  and  $W_F(t)$ .

### 3 RESULTS AND COMPARISON THEORY

Results are presented as percent difference between theory and experiment. Theory for steady cases are calm water ( $U_T, W_T=0$ ) and uniform flow ( $U_T=1, W_T=0$ ). Theory for unsteady data is 2D progressive-wave theory which characterizes the external flowfield with following equations

$$U_T = 1 + 2\pi f_w A e^{kz} \cos(kx - 2\pi f_e t) \quad (33)$$

$$W_T = 2\pi f_w A e^{kz} \sin(kx - 2\pi f_e t) \quad (34)$$

The perturbation for headwave flowfield is computed by subtracting the non-dimensional advance speed of the carriage ( $U_c=1$ ) from equation (33).

#### 3.1 Steady (calm water) with and without forward speed

Steady-flow data is presented for without and with forward speed conditions in Figs. 5 and 6a,b, respectively. For both cases, average comparisons theory and experiment over MA are summarized in Table 1 for WMA and NMA. Steady UA results from Gui et al. (2001c) are also included in Table 1 for comparison. The results include mean ( $U, V, W$ ) and turbulence ( $\overline{uu}, \overline{vv}, \overline{ww}, \overline{uv}, \overline{uw}$ )

parameters.

For  $U_c=0$  m/s, contours ( $U_T-U_E$ ) display a random pattern and magnitude is two orders less than axial velocity uncertainty ( $U_U$ ). Turbulence levels are several order-of-magnitude less than uncertainty values for ship flowfield.

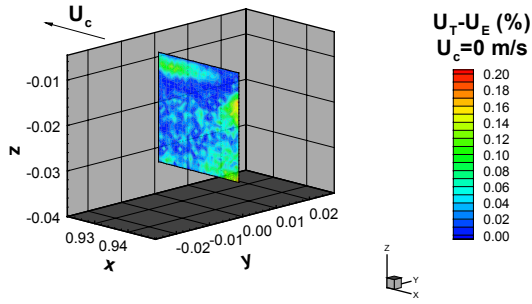


Fig. 5. Comparison (theory-experiment) of mean axial flow for  $U_c=0$  m/s

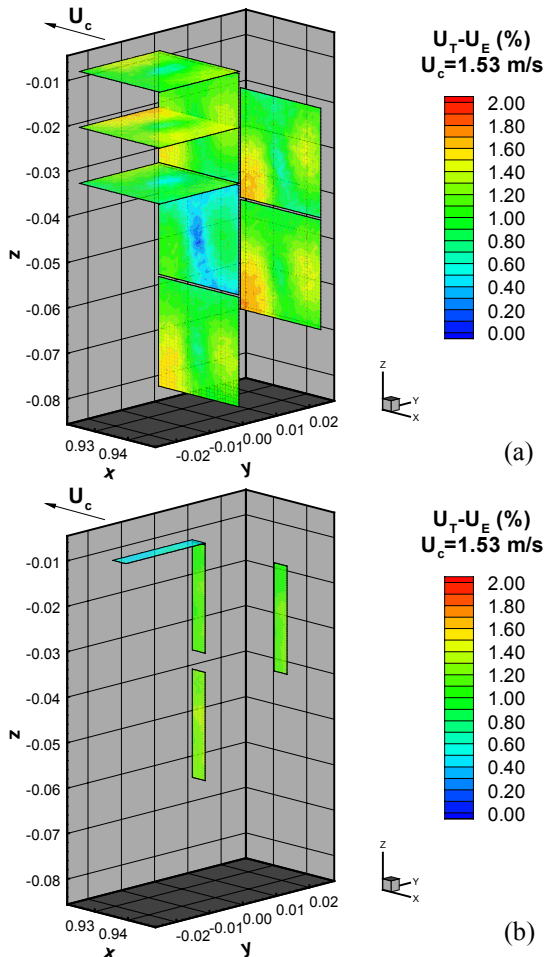


Fig. 6. Comparison (theory-experiment) of mean axial flow for  $U_c=1.53$  m/s: (a) WMA and five xz elevations and three xy elevations; (b) NMA and three xz elevations and one xy elevation.

For  $U_c=1.53$  m/s and WMA, contours ( $U_T-U_E$ ) for both

xz and xy configurations display organized, repeatable patterns independent of z or configuration with cells of decelerated flow at leading and trailing edge of MA. Origin of patterns are unknown but are thought to be consequence of either optical distortion of digital images or induced flow about PIV underwater torpedoes, or both. The former theory was tested by imaging standard grids, but no detectable distortion in the test images was observed. Also of interest is that potential-flow calculations for the PIV underwater torpedoes in a uniform flow do not replicate trends observed in Fig. 6a. For NMA (Fig. 6b), contour patterns ( $U_T-U_E$ ) have increased uniformity since focus area is a narrow strip centered on WMA. Absolute value ( $U_T-U_E$ ) roughly same in comparison WMA and turbulence levels are same order as for WMA but somewhat reduced.  $U_c=0$  m/s and 1.53 m/s results set the mean and turbulence noise levels of the fixed and towed PIV system, respectively. For the former, mean-flow levels are roughly 0.05%, 0.0005% for U, W, respectively, and for the latter levels are roughly 1-2 order-of-magnitude larger. Turbulence levels for both cases are very small but 2 orders-of-magnitude larger for the case with forward speed.

Table 1. Summary of comparison theory and experiment for steady PIV results with and without forward speed and  $z=-25$  mm.

	WMA		NMA	
	0 m/s	1.53 m/s	1.53 m/s	UA
U	0.05%	1.1%	1.1%	$U_U=2.4\%$
V	-	0.07%	0.3%	$U_V=7.7\%$
W	0.0004%	0.5%	0.080%	$U_W=4.4\%$
$\overline{uu}$	0.00003%	0.006%	0.004%	$U_{uu}=4.7\%$
$\overline{vv}$	-	0.003%	0.005%	$U_{vv}=4.3\%$
$\overline{ww}$	0.00002%	0.004%	0.004%	$U_{ww}=5.0\%$
$\overline{uv}$	-	0%	0.0005%	$U_{uv}=4.1\%$
$\overline{uw}$	0%	0.00042%	0.0002%	$U_{uw}=5.8\%$

### 3.2 Unsteady (waves) with and without forward speed

Unsteady-flow data is presented for without and with forward speed conditions in Fig. 7 and Figs. 8 through 12, respectively. For both cases, average comparisons theory and experiment over MA are summarized in Table 4 (WMA) and Table 5 (NMA). Tabulated results include comparisons theory and experiment for 0<sup>th</sup>-harmonic amplitude ( $U_0, V_0, W_0, \overline{uu}_0, \overline{vv}_0, \overline{ww}_0, \overline{uv}_0, \overline{uw}_0$ ), 1<sup>st</sup>-harmonic amplitude ( $U_1, V_1, W_1, \overline{uu}_1, \overline{vv}_1, \overline{ww}_1, \overline{uv}_1, \overline{uw}_1$ ), 2<sup>nd</sup>-harmonic amplitude ( $U_2, V_2, W_2, \overline{uu}_2, \overline{vv}_2, \overline{ww}_2, \overline{uv}_2, \overline{uw}_2$ ), 1<sup>st</sup>-harmonic phase ( $\gamma_{U1}, \gamma_{V1}, \gamma_{W1}, \gamma_{\overline{uu}_1}, \gamma_{\overline{vv}_1}, \gamma_{\overline{ww}_1}, \gamma_{\overline{uv}_1}, \gamma_{\overline{uw}_1}$ ), and 2<sup>nd</sup>-harmonic phase ( $\gamma_{U2}, \gamma_{V2},$

$\gamma_{W2}, \gamma_{\overline{uu}2}, \gamma_{\overline{vv}2}, \gamma_{\overline{ww}2}, \gamma_{\overline{uv}2}, \gamma_{\overline{uw}2}$ .

For  $U_c=0$  m/s, contours  $U_{0T}-U_{0E}, U_{1T}-U_{1E}, \gamma_{U1T}-\gamma_{U1E}$  (Fig. 7a,b,c) display random patterns through WMA. Magnitudes  $U_{0T}-U_{0E}$  and  $U_{1T}-U_{1E}$  are small everywhere and regarded satisfactory, especially in consideration of present orbital velocity magnitudes which are about  $5\%U_c$  for the wave parameters and measurement depth.  $\gamma_{U1T}-\gamma_{U1E}$  is also regarded satisfactory ( $\sim 1.1\%$ ) and positive everywhere which translates to a  $4^\circ$  phase lead.

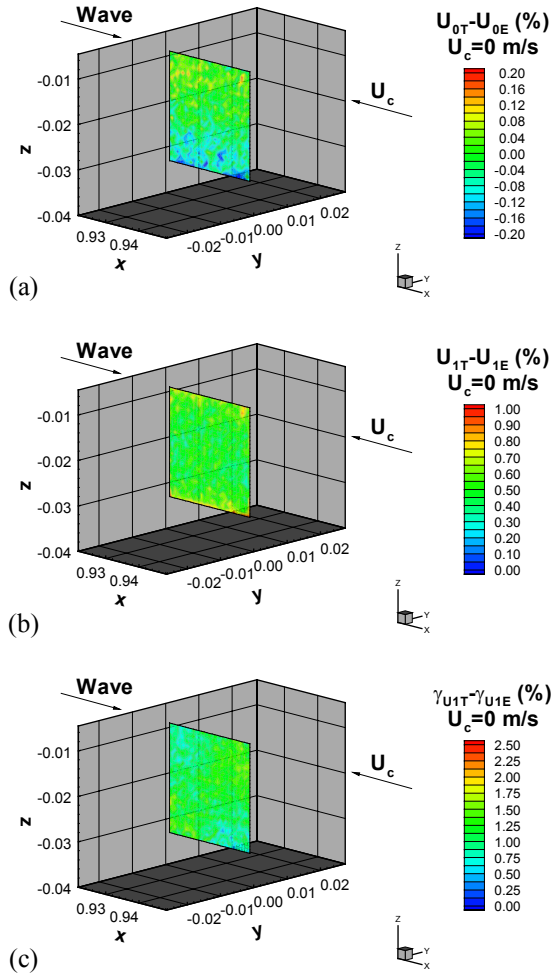


Fig. 7. Comparison (theory-experiment) of  $0^{\text{th}}$  and  $1^{\text{st}}$ -harmonic amplitude and  $1^{\text{st}}$ -harmonic phase  $U$  for  $U_c=0$  m/s and one elevation.

Comparisons for  $W$  variables are similarly satisfactory as shown in Table 4. Second harmonic amplitudes are order of  $1e-3$  for  $U_2$  and  $W_2$ , which is one order-of-magnitude smaller than  $U_1, W_1$  and indicates dominant  $1^{\text{st}}$ -harmonic response of flowfield to the incident wave. Turbulence FS amplitudes are nearly negligible everywhere, i.e., order of  $1e-5$  which is expected for case with no forward speed and carriage vibration. Turbulence FS phases are expressed as percentages of  $2\pi$ , but comparisons are difficult to interpret

due to noise in measurements. There are no xy-configuration data for case with zero forward speed.

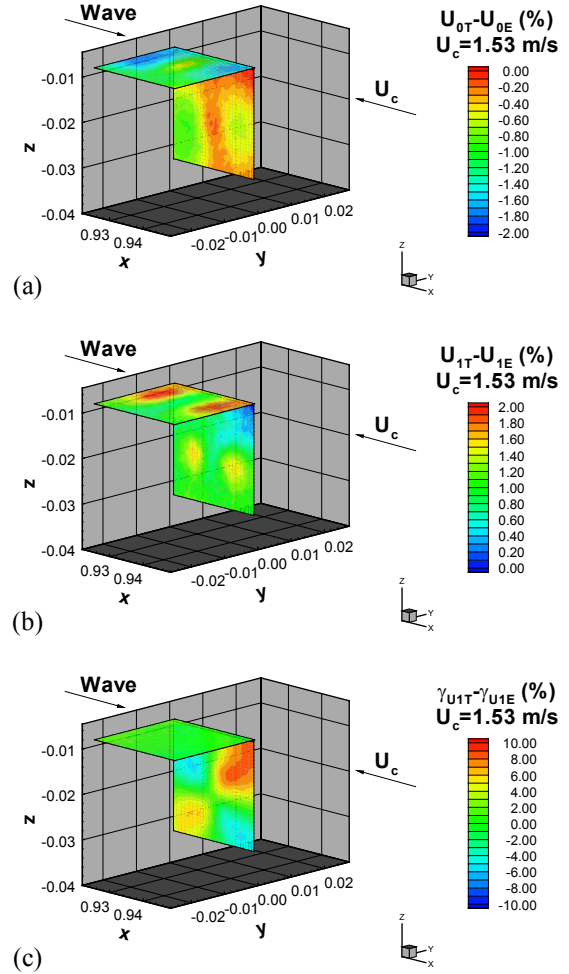


Fig. 8. Comparison (theory-experiment) of  $0^{\text{th}}$  and  $1^{\text{st}}$ -harmonic amplitude and  $1^{\text{st}}$ -harmonic phase  $U$  for  $U_c=1.53$  m/s and one elevation.

For  $U_c=1.53$  m/s, contours  $U_{0T}-U_{0E}, U_{1T}-U_{1E}, \gamma_{U1T}-\gamma_{U1E}$  (Fig. 8a,b,c) and  $\overline{uu}_{0T}-\overline{uu}_{0E}, \overline{uu}_{1T}-\overline{uu}_{1E}, \gamma_{\overline{uu}1T}-\gamma_{\overline{uu}1E}$  (Fig. 9a,b,c) are presented. In Fig. 8a,b,c for both xz and xy configurations, contours are changed and show organized, repeatable patterns. Origin of the patterns are unknown but also could be consequence of either optical distortion of digital images or an unsteady, induced flow about PIV underwater torpedoes, or both. No CFD was undertaken to determine if the observed patterns could be simulated.  $0^{\text{th}}$ -harmonic amplitude trends are similar in shape and magnitude with those observed in Fig. 6a, i.e., the uniform-flow perturbation pattern is recovered.  $U_{0T}-U_{0E}$  is roughly order-of-magnitude larger than for case with zero forward speed which is probably a result of both patterns in the data and carriage vibration.

$U_{1T}-U_{1E}$  is dominated in both xz and xy-configuration data by two circular cells downstream and upstream of

WMA leading and trailing edges, respectively, where  $U_{IE}$  is decreased.  $U_{IT}-U_{IE}$  is roughly twice value of case with zero forward speed which is again, probably a result of both patterns in the data and carriage vibration. Phase comparison ( $\gamma_{UIT}-\gamma_{UIE}$ ) displays phase leads and lags in a quadrant pattern where best agreement theory is within a cross pattern centered on WMA. Average ( $\gamma_{UIT}-\gamma_{UIE}$ ) is 2.4% or about an 8.5% phase lead.

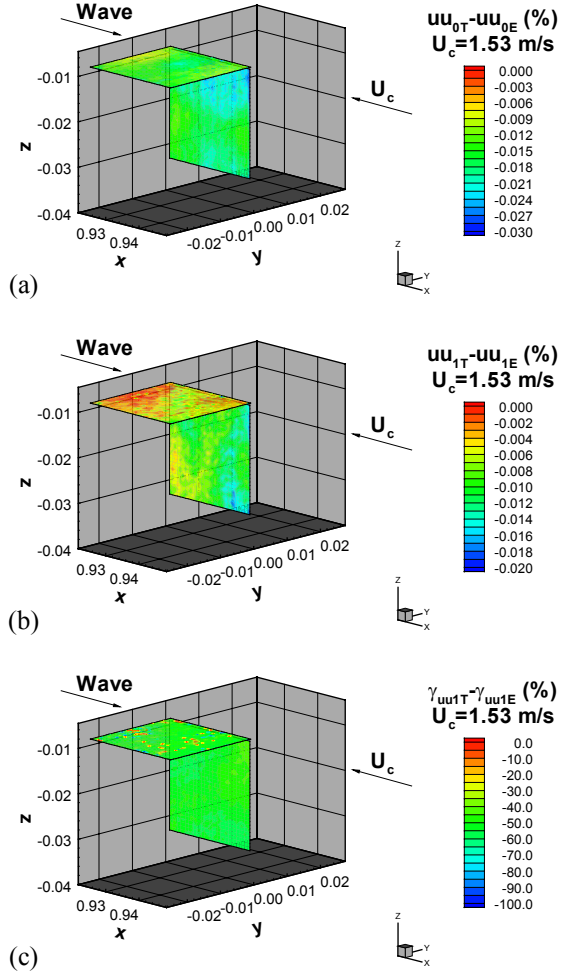


Fig. 9. Comparison (theory-experiment) of 0<sup>th</sup> and 1<sup>st</sup>-harmonic amplitude and 1<sup>st</sup>-harmonic phase  $\overline{uu}$  for  $U_c=1.53$  m/s and one elevation.

Similar comparisons as above for  $V, W$  are same order and also considered satisfactory as shown in Table 4. Of note is that  $V_1$  is not negligible, but small and confirms 2D nature of flowfield. Also, ( $\gamma_{VIT}-\gamma_{VIE}$ ) is roughly 50% which suggests that the small amount of  $V_1$  (0.8%) is excited at the midpoint, or trough, of each incident wave. As for previous case with  $U_c=0$  m/s, second harmonic amplitudes  $U_2, V_2, W_2$  are one order-of-magnitude smaller than 1<sup>st</sup>-harmonic amplitudes  $U_1, V_1, W_1$  confirming dominant 1<sup>st</sup>-harmonic response of measured data with moving carriage.

Turbulence FS amplitude and phase (Fig. 9a,b,c) patterns are mainly random through the MA. Although harmonic amplitudes are small, average values are one order-of-magnitude higher than for case with  $U_c=0$  m/s which could be due to carriage vibration. Of note is that 1<sup>st</sup>-harmonic phase differences for all turbulence variables are close to  $\pi$  (50% of  $2\pi$ ) which suggests again that the midpoint or trough of each incident wave is associated with higher levels of turbulence. In fact, according to 2D progressive wave theory, the trough region is a point where the axial and vertical pressure gradients ( $p_x$  and  $p_z$ ) are zero and maximum favorable, respectively. It is also a point of transition in the flow from accelerating  $U$  to decelerating  $U$  and downward  $W$  to upward  $W$ , thus a region experiencing higher flow stresses and consequently higher measured turbulence values. This effect is illustrated clearly in Fig. 4f which shows the axial normal stress distribution through one 0- $2\pi$  cycle at an arbitrary grid point and tendency for valid normal stress data to cluster near  $\pi$ .

Patterns and trends in Fig. 8 indicate that best comparison with theory occurs in a subregion (NMA) centered on WMA. Results for this region are shown in Figs. 10 and 11 for  $U$  and  $W$ , respectively, and Table 5. As expected, contours of comparisons theory and experiment for 0<sup>th</sup>- and 1<sup>st</sup>-harmonic amplitude and 1<sup>st</sup>-harmonic phase are uniform throughout NMA. Additionally, comparison values theory and experiment for 0<sup>th</sup>- and 1<sup>st</sup>-harmonic amplitudes and phases of  $U, W$  are reduced for NMA. 2<sup>nd</sup>-order effects in the harmonics of  $U, W$  are also reduced which indicates a cleaner linear response of the flowfield in the NMA. Also, harmonic content in the turbulence variables for NMA is reduced in comparison with WMA. Finally, flowfield vectors at four instances in one encounter period for  $z=-25.0$  mm are shown in Fig. 12 for theory and experiment. The vectors are colored with the vector magnitude to compare theoretical and experimental harmonic amplitude. Closeness of phase agreement is assessed by comparing vector direction between theory and experiment for any time instant. Through the range of  $z$ , amplitude comparison between theory and experiment is satisfactory. As expected, the vectors rotate through  $2\pi$  in one encounter period. Comparison of vector direction between theory and experiment for any instant is also satisfactory and phase or direction comparison is also satisfactory.

Based on the NMA data, Figs. 10 through 12 and Table 5 demonstrate good agreement with theory and are considered benchmark performance levels for towed, unsteady PIV at IIHR, i.e., approximately within 1% theory for 0<sup>th</sup>- and 1<sup>st</sup>-harmonic amplitude and within 1-2% theory for 1<sup>st</sup>-harmonic phase. As such, investigations of the unsteady nominal wake flowfield for model 5512 can move forward using the NMA and same DA/DR procedures documented herein.

4. CONCLUSIONS AND FUTURE WORK

Phase-averaged towed PIV measurements are made for regular head waves in a model-ship towing tank using both fixed and towed PIV systems in preparation for tests with model ships. Data reduction and uncertainty assessment software are developed and tested for both calm water and long wave, low steepness conditions used in previous tests with surface combatant. The results are validated through comparisons with progressive-wave theory.

Steady-flow results indicate random and organized patterns for cases without and with forward speed, respectively. Average comparisons with theory are roughly within 0.05%,0.0005% for U,W for the former and 1.0%,0.1% for U,W for the latter. Turbulence values are nearly negligible for both cases. All results are well within previous steady-flow UA results. Unsteady-flow results also display random and organized patterns in the FS harmonic amplitudes and 1<sup>st</sup>-harmonic phase for cases without and with forward speed, respectively.

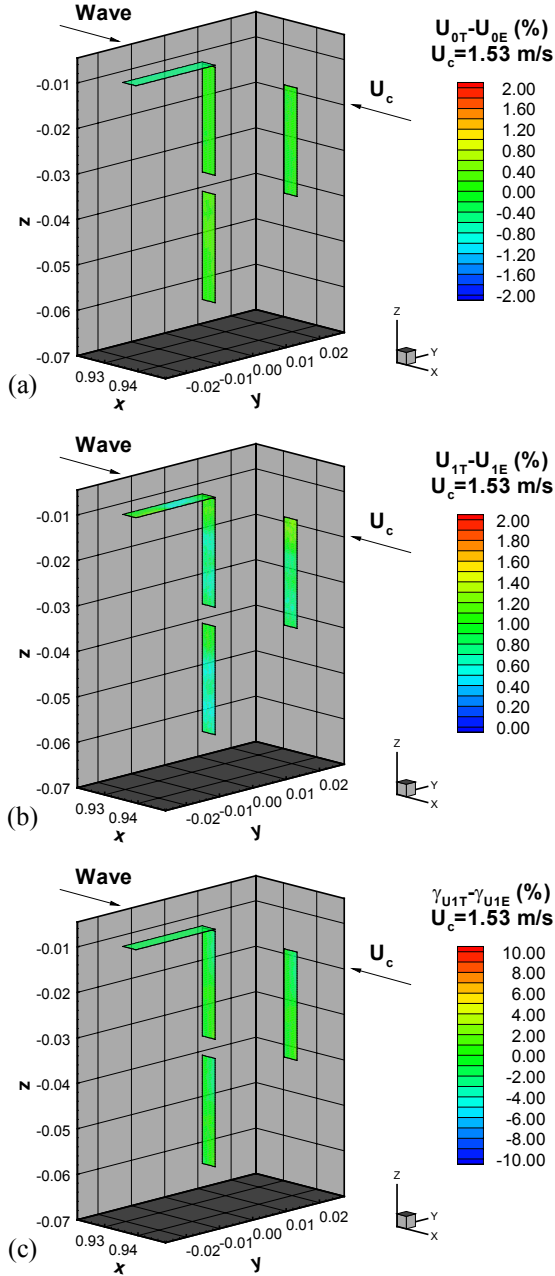


Fig. 10. Comparison (theory-experiment) of 0<sup>th</sup> and 1<sup>st</sup>-harmonic amplitude U for  $U_c=1.53$  m/s and 1<sup>st</sup>-harmonic phase U for three elevations.

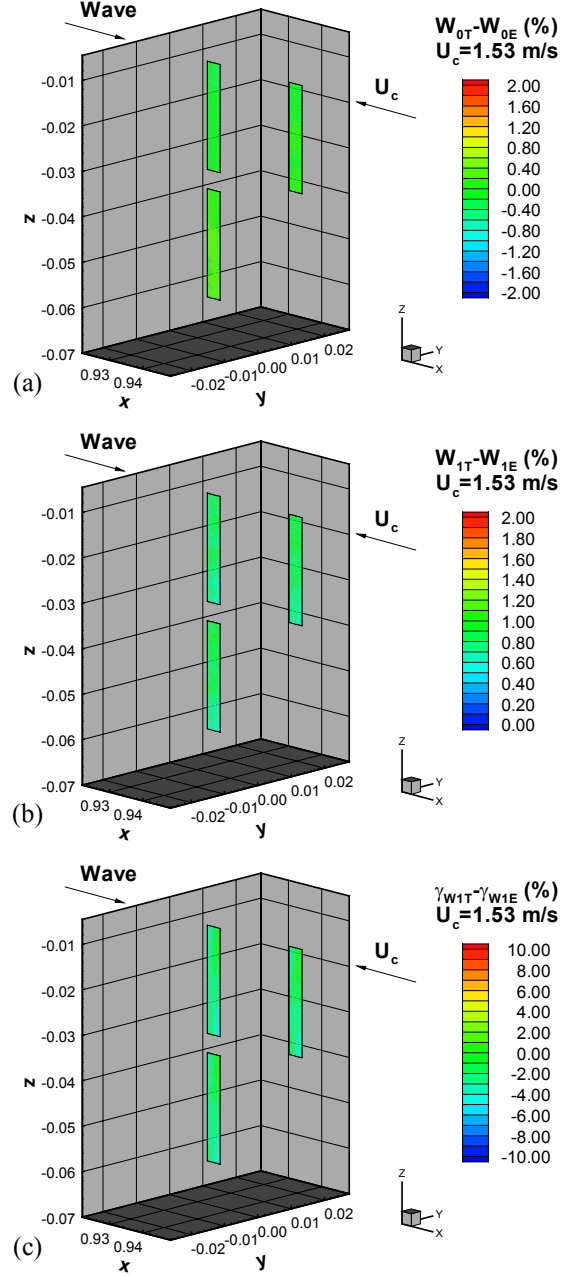


Fig. 11. Comparison (theory-experiment) of 0<sup>th</sup> and 1<sup>st</sup>-harmonic amplitude W for  $U_c=1.53$  m/s and 1<sup>st</sup>-harmonic phase W for three elevations.

Best average comparisons with 2D progressive-wave theory are roughly within 1% for the 0<sup>th</sup>- and 1<sup>st</sup>-harmonic amplitude and 1-2% for the 1<sup>st</sup>-harmonic phase and occur inside a narrow window centered on the PIV object plane.

The origin of the patterns that emerge with forward speed in the steady and unsteady flow are unknown. Efforts to understand the source of the patterns included testing of the digital images and potential-flow calculations of the flow around the PIV torpedoes for the steady case but both were inconclusive. The prevailing theory for these patterns is sub-pixel distortion in the digital images, induced flow by the underwater PIV torpedoes, or a combination of both.

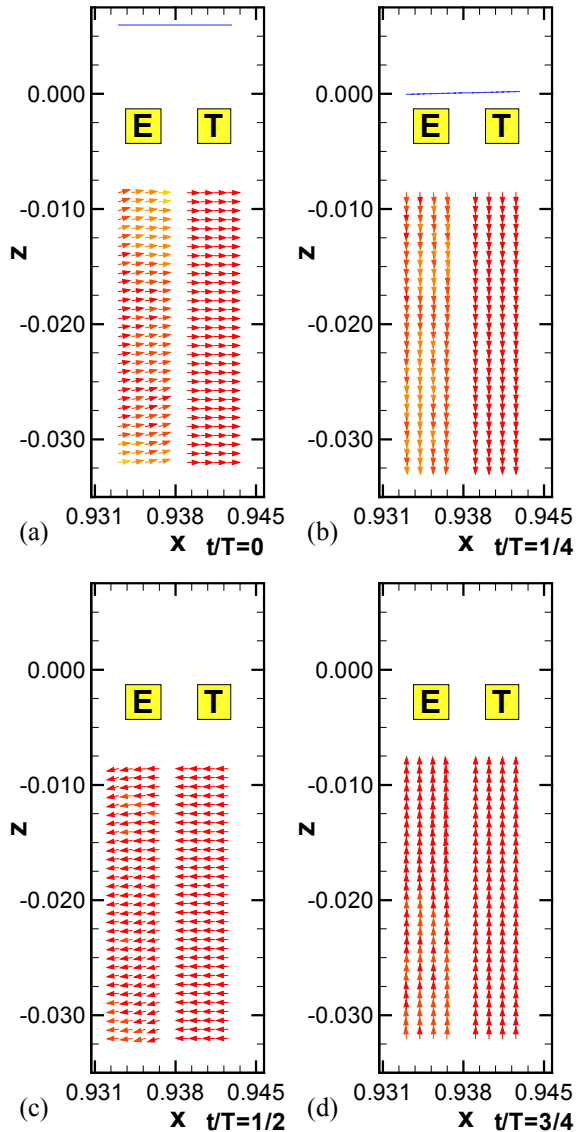


Fig. 12. Flowfield vectors at four instances in one encounter period.

Future work includes steady and unsteady PIV measurements and full UA of the nominal wake plane of model 5512 for same long wavelength, low wave steepness incident wave presented herein. Documentation of the test

program and results are ongoing (Longo et al., 2002). The data and UA will be archived at [www.iihr.uiowa.edu~towtank](http://www.iihr.uiowa.edu~towtank).

#### ACKNOWLEDGEMENTS

This research was sponsored by Office of Naval Research under Grants N00014-96-1-0018 under the administration of Dr. E.P. Rood and N00014-01-1-0073 under the administration of Dr. Pat Purtell whose support is greatly appreciated.

#### REFERENCES

- ASME, (1998), "Test Uncertainty," ASME PTC 19.1-1998, The American Society of Mechanical Engineers, 112 pp.
- Gui, L., Longo, J., and Stern, F., (2001a), "Biases of PIV Measurement of Turbulent Flow and the Masked Correlation-Based Interrogation," *Experiments in Fluids*, Vol. 30, Issue 1, pp. 27-35.
- Gui, L., Longo, J., and Stern, F., (2001b), "Towing Tank PIV Measurement System, Data and Uncertainty Assessment for DTMB Model 5512," *Experiments in Fluids*, Vol. 31, pp. 336-346.
- Gui, L., Longo, L., Metcalf, B., Shao, J., and Stern, F., (2001c), "Forces, Moment, and Wave Pattern for Surface Combatant in Regular Head Waves-Part 1: Measurement Systems and Uncertainty Analysis," *Experiments in Fluids*, Vol. 31, Issue 6, pp. 674-680.
- Gui, L., Longo, L., Metcalf, B., Shao, J., and Stern, F., (2002), "Forces, Moment, and Wave Pattern for Naval Combatant in Regular Head Waves-Part 2: Measurement Results and Discussions," *Experiments in Fluids*, to appear.
- Journee J M J (1992), Experiments and calculations on four Wigley hullforms. Delft University of Technology, Ship Hydromechanics Lab, Report No. 909.
- Longo, J., Shao, J., Irvine, M., and Stern, F., (2002), "Phase-averaged PIV for Surface Combatant in Regular Head Waves," 24<sup>th</sup> Symposium on Naval Hydrodynamics, Fukuoka, Japan (in preparation).
- Rhee, S.H. and Stern, F., (2001), "Unsteady RANS Method For Surface Ship Boundary Layer And Wake And Wave Field," *Int. J. Num. Meth. Fluids*, Vol. 37, pp. 445-478.
- R. Wilson and F. Stern, (2002), "Forward Speed Diffraction Problem for a Naval Surface Combatant using an Unsteady RANS Method," 24<sup>th</sup> Symposium on Naval Hydrodynamics, Fukuoka, Japan (in preparation).
- Stern F, Longo J, Penna R, Oliveira A, Ratcliffe T, Coleman H (2000), International Collaboration on Benchmark CFD Validation Data for Naval Surface Combatant. 23<sup>rd</sup> ONR Symposium on Naval Hydrodynamics, Val de Reuil, France, 17-22 September.

Table 4. Summary of comparison theory and experiment for unsteady PIV results with and without forward speed for WMA and  $z=-25$  mm.

	$U_c=0$ m/s			$U_c=1.53$ m/s		
	<b>Amplitude (theory-experiment) x 100%</b>					
	$0^{th}$	$1^{st}$	$2^{nd}$	$0^{th}$	$1^{st}$	$2^{nd}$
$U$	0.1	0.5	0.2	0.9	1.1	0.1
$V$	-	-	-	0.1	0.8	0.1
$W$	0.1	0.3	0.1	0.4	1.5	0.2
$\overline{uu}$	0.006	0.002	0.004	0.02	0.007	0.007
$\overline{vv}$	-	-	-	0.008	0.003	0.005
$\overline{ww}$	0.004	0.002	0.001	0.01	0.007	0.004
$\overline{uv}$	-	-	-	0.001	0.003	0.002
$\overline{uw}$	0.0004	0.0008	0.001	0.003	0.006	0.002
	<b>Phase (theory-experiment) x 100%</b>					
	$0^{th}$	$1^{st}$	$2^{nd}$	$0^{th}$	$1^{st}$	$2^{nd}$
$U$	18.1	1.1	43.7	0	2.4	47.3
$V$	-	-	-	39.3	55.3	52.5
$W$	2.5	0.7	48.1	0	3.2	57.7
$\overline{uu}$	0	32.2	71.3	0	51.0	63.5
$\overline{vv}$	-	-	-	0	49.7	68.1
$\overline{ww}$	0	23.2	55.2	0	60.9	51.0
$\overline{uv}$	-	-	-	18.8	52.6	52.8
$\overline{uw}$	18.0	49.4	70.5	26.3	63.2	46.1

Table 5. Summary of comparison theory and experiment for unsteady PIV results with forward speed for NMA and two elevations.

	$z=-25$ mm			$z=-53.34$ mm		
	<b>Amplitude (theory-experiment) x 100%</b>					
	$0^{th}$	$1^{st}$	$2^{nd}$	$0^{th}$	$1^{st}$	$2^{nd}$
$U$	0.30	0.8	0.08	0.05	0.9	0.06
$V$	0.27	0.4	0.03	-	-	-
$W$	0.12	0.8	0.06	0.06	0.8	0.05
$\overline{uu}$	0.01	0.006	0.004	0.01	0.006	0.003
$\overline{vv}$	0.007	0.0007	0.001	-	-	-
$\overline{ww}$	0.01	0.003	0.004	0.01	0.002	0.002
$\overline{uv}$	0.0006	0.0005	0.0004	-	-	-
$\overline{uw}$	0.0004	0.0009	0.0007	0.0005	0.0007	0.0007
	<b>Phase (theory-experiment) x 100%</b>					
	$0^{th}$	$1^{st}$	$2^{nd}$	$0^{th}$	$1^{st}$	$2^{nd}$
$U$	0	1.1	52.2	0	0.8	52.1
$V$	0	56.2	-	-	-	-
$W$	2.1	2.3	37.9	2.4	2.0	30.1
$\overline{uu}$	0	52.2	17.3	0	51.0	27.9
$\overline{vv}$	0	56.0	21.3	-	-	-
$\overline{ww}$	0	58.5	55.9	0	50.5	56.1
$\overline{uv}$	48.5	44.9	54.0	-	-	-
$\overline{uw}$	14.1	34.4	67.0	5.3	35.8	73.3